Jpn. J. Appl. Phys. Vol. 42 (2003) pp. 3950–3957
Part 1, No. 6B, June 2003
©2003 The Japan Society of Applied Physics

Structure of Latent Tracks Created by Swift Heavy Ions in Amorphous SiO_2 and Zinc Phosphate Glass

Koichi AWAZU*, Sjoerd ROORDA[1], John L. BREBNER[1,†], Satoshi ISHII[2] and Kunihiro SHIMA[2]

Photonic Research Institute, National Institute of Advanced Industrial Science and Technology (AIST), 1-1-1 Umezono, Tsukuba 305-8568, Japan
[1]*Groupe de Recherche en Physique et Technologie des Couches Minces (GCM), Département de Physique, Université de Montréal, P.O. Box 6128, Station "Centre-Ville", Montréal, Québec H3C 3J7, Canada*
[2]*Tandem Accelerator Center, University of Tsukuba, Tennoudai, Tsukuba 305-8577, Japan*

(Received November 1, 2002; revised manuscript received March 13, 2003; accepted for publication March 27, 2003)

The structure of latent tracks introduced by swift-heavy-ion irradiation was examined on both amorphous SiO_2 and zinc phosphate glass ($68P_2O_5$:25ZnO:$4.5Al_2O_3$:$2.5Na_2O$). In amorphous SiO_2, the frequency of the infrared absorption assigned to the asymmetric stretching vibration of Si–O decreased with irradiation. This IR peak shift has been found to be related to the transition of normal six-membered rings of SiO_4 tetrahedra to planar three-membered rings. The high etching rate of the latent tracks is strongly related to planar three-membered rings. In the ion-irradiated zinc phosphate glass, two bridging oxygen atoms bound to a phosphorus atom turned into one bridging oxygen atom. Scission of the Zn–O bond was not observed. It was concluded that the high etching rate of the latent tracks in zinc–phosphate glass is related to P–O bond scission.
[DOI: 10.1143/JJAP.42.3950]

KEYWORDS: amorphous SiO_2, zinc phosphate glass, metaphosphate glass, swift heavy ion, latent track, etching, XPS, FT-IR, Raman

1. Introduction

When a swift heavy ion passes through most insulators, its energy is reduced while creating a heavily damaged zone along its path. The damaged zone can be made visible by chemical etching, thus the ion path is called "latent track".[1)] Most of the earlier studies on what are concerned with the identification of both particle species and their energy by observation of the etched track diameter, made possible by the chemical etch rate along a particle track depends on projectile mass.[2)] In particular, zinc phosphate glass has been used to measure the energy spectra of fission fragments in the field of nuclear physics.[3)] For example, ^{252}Cf fission fragments were measured in phosphate glasses by determining the etching rate in alkaline or acid solutions.[3,4)] Other studies have focused on the very early stages of track formation and how excited electrons transfer energy to the network. The thermal spike model[5,6)] is one of the most widely accepted theories for describing how ion energy is transferred rapidly and locally, introducing extremely high temperatures along the ion path. Alternatively, in the ion spike or Coulomb explosion model,[3,7)] the ion track is considered to denude electrons long enough for the mutual Coulombic repulsion of neighboring atoms to occur. However, these models give little information on the structure of the latent track and on the atomic mechanism underlying the enhanced etch rate of the latent track. In the present study, we attempt to improve our understanding of these latter issues by approaching the problem from different angles, correlating changes of infrared absorption, Raman spectroscopy and X-ray photoelectron spectroscopy (XPS) results with etching enhancement in latent tracks. We chose amorphous SiO_2 (a-SiO_2) and zinc phosphate glass to examine the defects generated in the particle tracks because etched tracks can be observed in both materials[3)] yet the structure of the latent track and the mechanism underlying the generation of individual cones in these materials have not been investigated.

*Corresponding author. E-mail address: k.awazu@aist.go.jp
†Deceased.

2. Experimental

Amorphous SiO_2 films with thicknesses of 200 nm and 1 μm were grown on silicon wafers in dry O_2 or a mixture of O_2 and H_2 at 1000°C, respectively (hereafter, dry-SiO_2 and wet-SiO_2). Dry-SiO_2 of 810 nm thickness was also fabricated to examine the effect of film thickness on the infrared spectrum. The thermal oxide on the other side of a wafer was completely etched out with hydrofluoric acid before each irradiation. In order to observe etched tracks directly, 2-mm-thick a-SiO_2 plates of Type-III[8)] which was synthesized by chemical vapor deposition and contained 1000 ppm OH were used. $68P_2O_5$:25ZnO:$4.5Al_2O_3$:$2.5Na_2O$ glass (ZnP glass) was prepared from reagent-grade H_3PO_4 (85% aqua solution), $Al(OH)_3$, ZnO and Na_2CO_3. Raw materials were thoroughly mixed and grounded in water with mortar and pestle for 30 min to obtain a slurry. The slurry was dried in an oven at 125°C for 1 day. About 400 g of the dried powder was melted in a Pt crucible (300 cm^3) at 1250°C for 1 h, then the melt was poured onto a carbon plate for quenching, annealed at 390°C for 4 hr and cooled to room temperature in a furnace. The glass was cut into $20 \times 20 \times 2$ mm^3 plates and polished with SiC and CeO_2 powder to obtain a flat surface. The ZnP glass plates obtained were transparent without bubbles.

Ion bombardment was performed at room temperature and at a residual pressure below 1×10^{-4} Pa. We employed the 12 MV tandem accelerator of the University of Tsukuba to generate swift Br and I ions. 120 MeV Br^{11+} and 98 MeV I^{12+} beams passed through Au foils of 4 and 1.14 mg/cm^2 weight, and thus their mean energies decreased to 67 MeV and 80 MeV, respectively. At these energies, the ion fluences were high ranging from 1×10^{11} cm^{-2} to 1×10^{15} cm^{-2}.[9,10)] By comparison, the energies of the 127 MeV Br^{11+} and 112 MeV I^{13+} beams were reduced to 92 MeV and 76 MeV, respectively; their ion fluence was only 1×10^7 cm^{-2} for the observed etched tracks. The 6 MV Tandem accelerator of the Université de Montréal was also employed for the backscattered 30 MeV Si^{6+} ion beams.[11)] Figure 1(a) shows the schematic of the experimental setup for the backscattering of

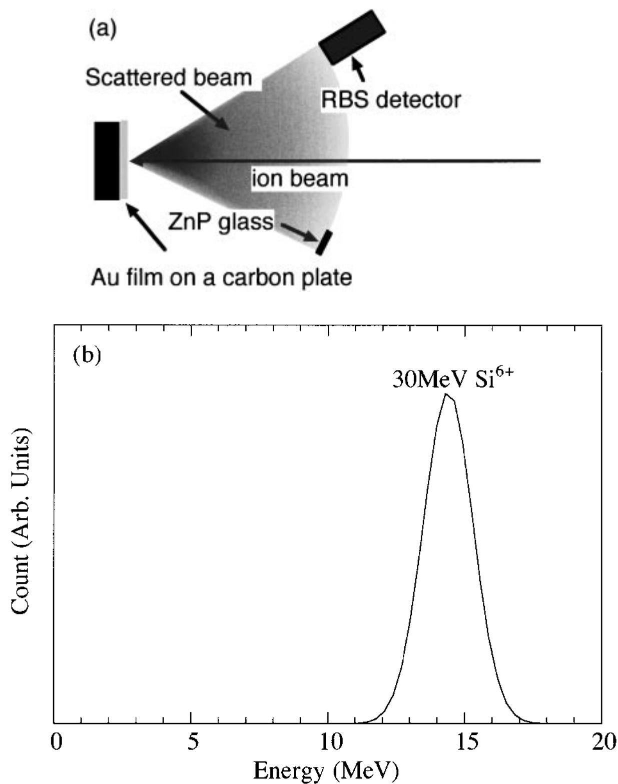

Fig. 1. (a) Alignment of the flux diffuser for 30 MeV Si irradiation. A perpendicular incident beam was reflected on a 1-μm-thick gold film, and reflected ions hit both the sample holder and an RBS detector for determining accumulated dose. (b) RBS signal for 30 MeV Si ions diffused with the system shown in (a).

Si ions. The collimated ion beam is incident at a normal angle to a 1-μm-thick Au film deposited by evaporation on a carbon plate. Since the total fluence required here was very small, the backscattering geometry was chosen in order to reduce the ion flux on the sample to an acceptable value. The particles scattered at a 30° angle bombarded the sample while the backscattered ions were simultaneously counted using a solid state nuclear detector at −30°. In this geometry, α particles from americium were used as an energy standard to determine the energy of the Si ions. Figure 1(b) shows the energy distribution of the backscattered Si ions. Note that the backscattered ions have a maximum energy of 14.4 MeV with a full width at half maximum of 1.8 MeV.

The etching rate for a-SiO_2 subjected to irradiation was determined as follows. An a-SiO_2 film partly covered with a silicon wafer was irradiated, then etched with hydrofluoric acid. The step height between the irradiated and masked parts was measured with a surface profilometer. Chemical etching for track observation in a-SiO_2 and ZnP glasses was performed with 48% hydrofluoric acid and 12 N NaOH solution at room temperature for 45 s and 1 h, respectively.

Infrared absorption was measured with a Fourier transform IR (FT-IR) spectrophotometer (Shimadzu FT-IR8200). The surface morphology of the samples was observed with a scanning electron microscope (SEM; JSM T-300, JEOL). XPS was performed with a Vacuum Generators ESCA-3 spectrometer using a MgKα source ($h\nu = 1253.6$ eV). During the experiments, the pressure inside the analysis chamber was about 10^{-7} Pa. The spectra were calibrated using the binding energy of 284.5 eV of the C_{1s} peak, which is always present. Raman spectroscopy was performed with an Ar^+ laser operating at 488 nm. The incident laser light was nearly parallel to the ion-irradiated surface, thus probing a 50-μm-thick region below the top surface.

3. Results

3.1 *Amorphous SiO_2*

Figure 2 shows an SEM micrograph of an a-SiO_2 plate irradiated with 92 MeV Br ions at an accumulated dose of $1 \times 10^7\,cm^{-2}$ and subsequently etched with 48% hydrofluoric acid for 20 s. The sample was tilted 45° with respect to the incident electron beam. The right-hand side (bright area) is the surface on which Br ions were launched perpendicularly. In order to observe the cross section of the etched track, the plate was scratched with a diamond-point pen after etching and one such scratch is visible along the left edge of the micrograph. The etched track has a conical shape with a maximum diameter of 800 nm and a depth of 1.2 μm.

Figures 3(a) and 3(b) show the IR absorption spectra of the dry-SiO_2 and wet-SiO_2 irradiated with 67 MeV Br ions. In Fig. 3(a), there are two peaks in the IR absorption of pristine dry-SiO_2 at $1078\,cm^{-1}$ and at $805\,cm^{-1}$ labelled ω_4 and ω_3, respectively, assigned to Si–O asymmetric vibration and bending, respectively. A decrease in ω_4 from $1078\,cm^{-1}$ to $1044\,cm^{-1}$ and an increase in ω_3 from $807\,cm^{-1}$ to $822\,cm^{-1}$ were simultaneously observed with an increase in accumulated ion fluence. Note that ω_4 and the width of ω_4 for wet-SiO_2 are different from those for dry-SiO_2. In wet-SiO_2, ω_4 decreased from $1092\,cm^{-1}$ to $1060\,cm^{-1}$ and ω_3 increased from $807\,cm^{-1}$ to $822\,cm^{-1}$ with accumulated ion fluence.

In order to compare the difference in peak frequency between dry-SiO_2 and wet-SiO_2, the shifts in ω_4 from $1078\,cm^{-1}$ for dry-SiO_2 and $1092\,cm^{-1}$ for wet-SiO_2 were plotted as a function of accumulated dose and depicted in Fig. 4. Closed and open circles denote frequencies of dry-SiO_2 and wet-SiO_2 subjected to 67 MeV Br irradiation and closed and opened triangles subjected to 80 MeV I irradiation, respectively. The frequencies of all samples were reduced and subsequently became stable after a shift of $-33\,cm^{-1}$ for both a-SiO_2 films.

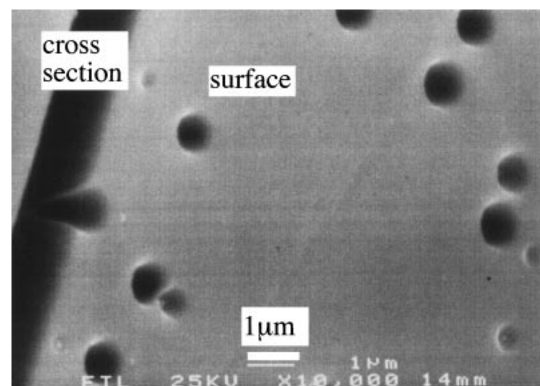

Fig. 2. SEM observation of a-SiO_2 plate subjected to 92 MeV Br irradiation at an accumulated dose of $1 \times 10^7\,cm^{-2}$ followed by etching with 48% hydrofluoric acid for 45 s. Observation was carried out at incident angle of 45°.

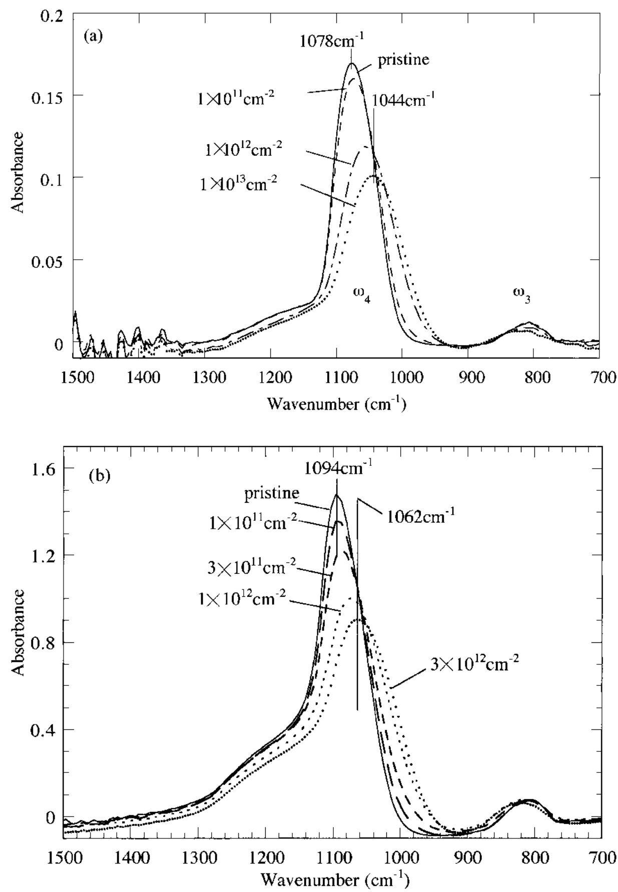

Fig. 3. Evolution of IR absorption spectra of a-SiO_2 of 200 nm thickness (dry-SiO_2, (a)) and of 1 μm thickness (wet-SiO_2, (b)) subjected to 67 MeV Br irradiation with increase in the accumulated dose.

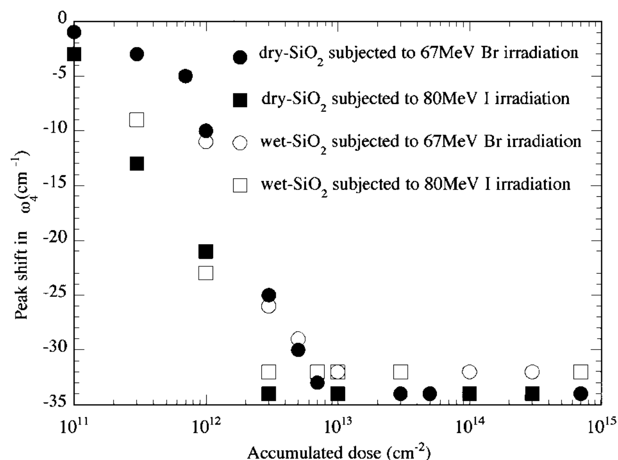

Fig. 4. Peak shift in ω_4 of dry-SiO_2 (closed symbols) and wet-SiO_2 (open symbols) subjected to 67 MeV Br (circles) and 89 MeV I (squares) irradiations plotted against the accumulated dose.

Figure 5 shows a plot of the etch rate, normalized to unity for the unirradiated case, versus accumulated dose. Closed triangles, squares, circles, diamonds and reversed triangles present the etch rates of wet-SiO_2 subjected to 2 MeV Li, 4 MeV C, 30 MeV Si, 67 MeV Br and 78 MeV I irradiations, respectively. In all cases, the etch rate increased, then reached a maximum value, and finally decreased with accumulated dose. Open symbols depicted in the figure will be mentioned in the discussion section.

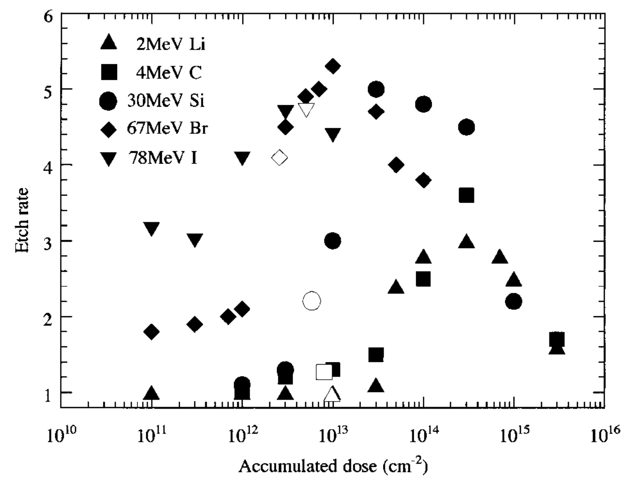

Fig. 5. Relative etching efficiencies of wet-SiO_2 subjected to 2 MeV Li, 4 MeV C, 30 MeV Si, 67 MeV Br and 78 MeV I irradiations, denoted by closed triangles, squares, circles, diamonds and reversed triangles, respectively, plotted against shift in ω_4. Open symbols on each marks represent etching rate at MDDZ.

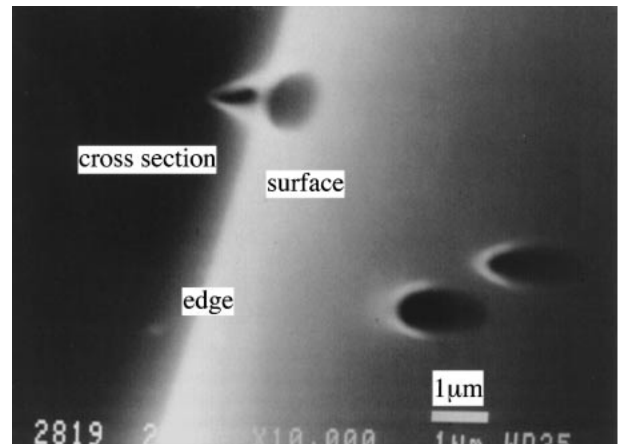

Fig. 6. SEM observation of ZnP glass irradiated with 14.4 MeV Si of 1×10^7 ions/cm^2 followed by etching for 1 h. Observation was performed at a 45° off-normal position. In order to observe the cross section of the etched track, the surface of the glass was scratched with a diamond-point pen after etching.

3.2 ZnP glass

Figure 6 shows an SEM micrograph of the ZnP glass irradiated with 14.4 MeV Si ions at an accumulated dose of 1×10^7 ions/cm^2 followed by etching with 12 N NaOH solution for 1 h. SEM was again performed at 45° off-normal to clearly observe the cross-section of each hole. Cores of 1 μm diameter and 1.5 μm depth were observed. In particular, it was possible to observe the entire shape of an etch pit located near the edge of the sample.

Figures 7(a)–7(c) show the change in the XPS line shape of the P_{2p}, O_{1s} and Zn_{2p} peaks in ZnP glass by the following subsequent ion bombardment. All spectra are normalized to a constant maximum intensity. The solid and dotted lines in the P_{2p} and O_{1s} spectra denote pristine ZnP and ZnP subjected to 14.4 MeV Si irradiation at an accumulated dose of 1×10^8 ions/cm^2. The three lines all behave differently under ion irradiation: the P_{2p} spectrum broadens with addition of a shoulder in the region of 133 eV (see Fig.

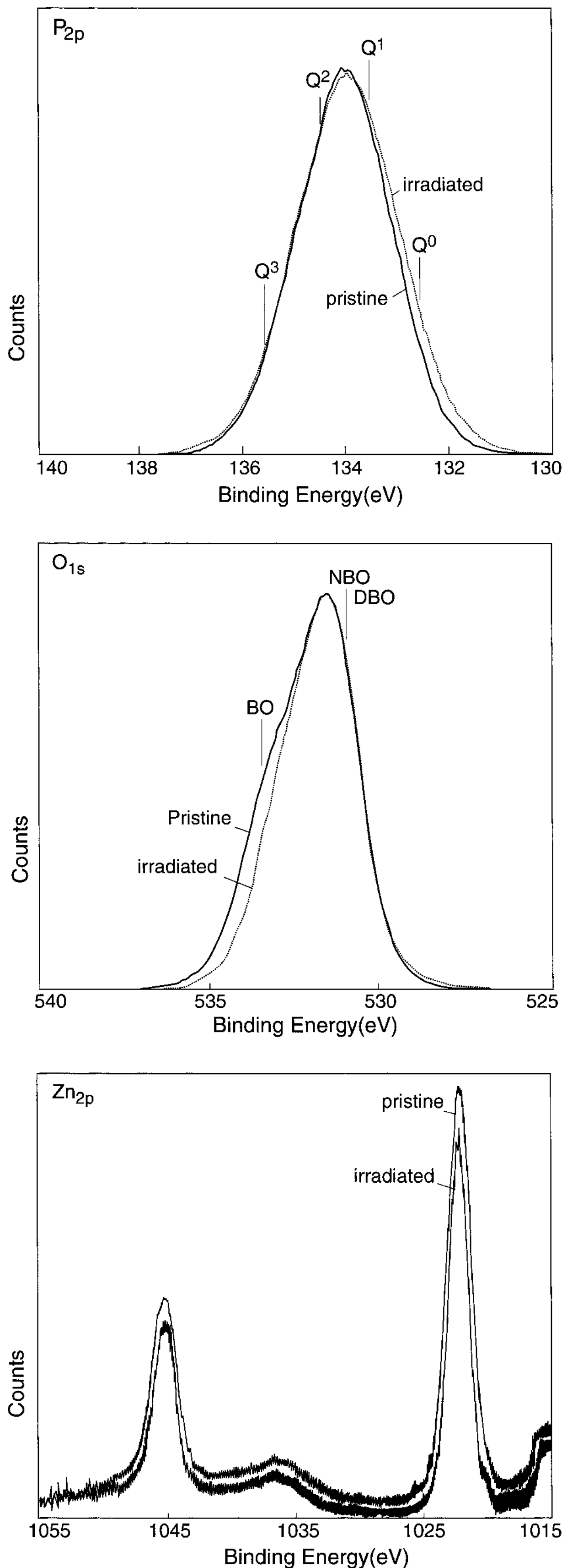

Fig. 7. XPS spectra of samples irradiated with 14.4 MeV Si ions of 1×10^8 ions/cm^2 of P_{2p}, O_{1s} and Zn_{2p}. Solid and dotted lines in P_{2p} and O_{1s} spectra denote the pristine ZnP and irradiated ZnP glass, respectively. The upper and lower spectra in Zn2p spectra denote the virgin ZnP and irradiated ZnP glass, respectively.

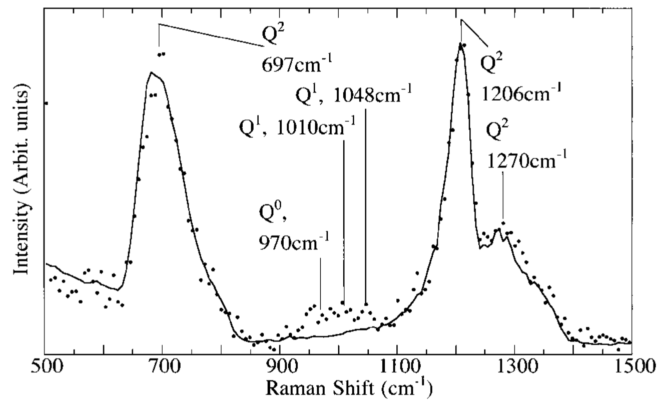

Fig. 8. (a) Raman spectra of pristine (solid line) and irradiated ZnP with 14.4 MeV Si at an accumulated dose of 1×10^8 cm^{-2} (dotted line).

7(a)), the O_{1s} spectrum narrows with the lost of a shoulder in the region of 534 eV (see Fig. 7(b)), and no change was observed in the Zn_{2p} spectrum other than a uniform change in yield over the entire spectral range.

Figure 8 shows Raman signals from a pristine ZnP sample (solid line) and a sample irradiated with 1×10^8 ions/cm^2, 14.4 MeV Si (dotted line). The pristine sample was measured in two geometries, probing both the bulk and a 50-µm-thick layer near the top surface. These geometries gave identical Raman spectra with a difference only in the signal-to-noise ratio. Three peaks were observed, i.r., at 697 cm^{-1}, 1206 cm^{-1}, and 1270 cm^{-1}. After irradiation, these peaks were still present but in addition, broad and weak bands were generated in the vicinity of 1000 cm^{-1}.

4. Discussion

4.1 Amorphous SiO_2

It is widely accepted that a-SiO_2 is composed of n-membered rings of SiO_4 tetrahedra, where "n-membered rings" means n Si atoms and n O atoms in a loop.[12] The irregularity of these rings is associated with the broad distribution of the Si–O–Si angle (θ_n) in planar rings of order n. By comparison, the O–Si–O angle ϕ is found much more narrowly distributed around a tetrahedral value ϕ of 109.5°. A schematic model of the tetrahedra arranged in a planar ring of order n, identifying angles θ_n and ϕ, is shown in Fig. 9(a).[12]

Newton and Gibbs have carried out *ab-initio* SCF-MO calculations and their results are shown in Fig. 9(b).[13] In accordance with Galeener, the bond angles have all been shifted by 10° so that the minimum energy is located at the most probable value for a-SiO_2, $\theta = \langle\theta\rangle$.[12] Once an n-membered ring is generated, it attempts to minimize energy by changing θ values toward the lowest energy $\langle\theta\rangle$. Thus, a puckered ring of order n having θ less than $\langle\theta\rangle$ can increase its θ value by "unpuckering" to be planar. In contrast, planar rings of order n having θ greater than $\langle\theta\rangle$ will tend to pucker so as to reduce their energy. Of course, not every θ will achieve $\langle\theta\rangle$ because of steric hindrance.

It has been reported that the ω_4 depends on the average bond angle θ and, in good approximation, is:[14,15]

$$\omega_4 = a[2(\alpha \sin^2 \theta/2 + \beta \cos^2 \theta/2)/m]^{1/2}, \qquad (1)$$

where α and β are the central and non-central force

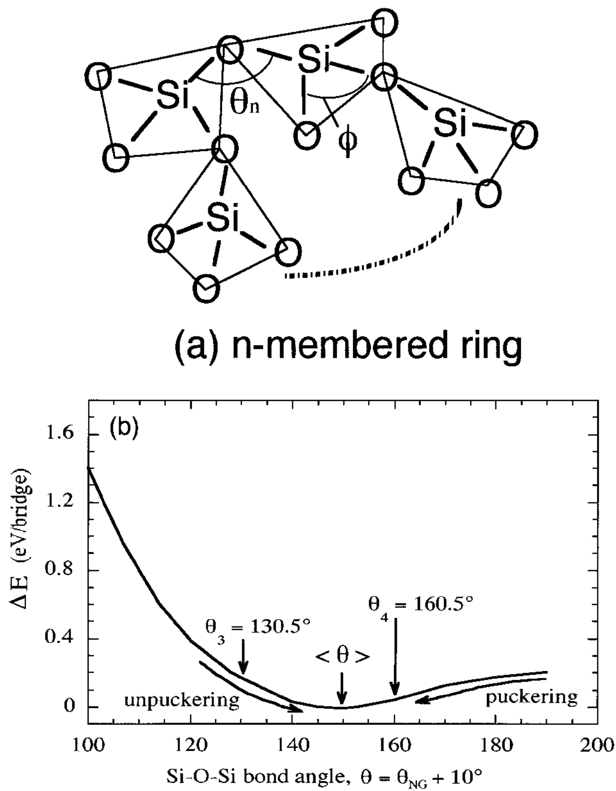

Fig. 9. Structure of a-SiO_2 composed of SiO_4 tetrahedra. Si–O–Si bond angles in n-membered rings (θ_n) are widely distributed. By comparison, the O–Si–O bond angle (ϕ) is rigid. (b) Dependence of the energy of a Si–O–Si bridge on bridge angle θ, as estimated by Newton and Gibbs.[13] Original data in this figure cited from ref. 12.

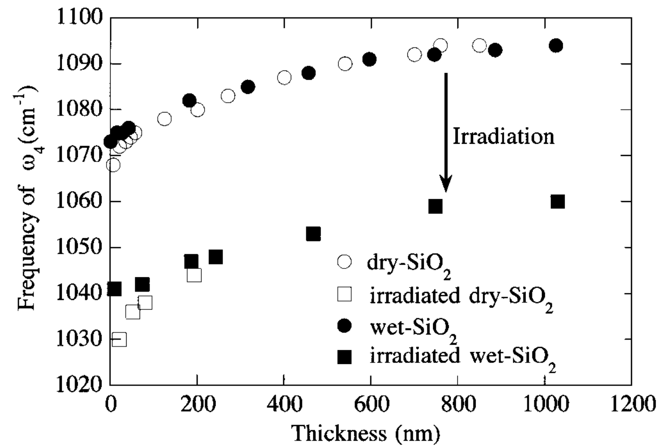

Fig. 10. Plots of ω_4 against the thicknesses of dry-SiO_2 (open circles) and wet-SiO_2 (closed circles). The relationship was obtained with repeated etching using hydrofluoric acid and IR measurement at each step. Open and closed circles represent the thicknesses of dry-SiO_2 and wet-SiO_2 without irradiation, respectively. Open and closed squares denote the thicknesses of dry-SiO_2 and wet-SiO_2 subjected to 67 MeB Br irradiation and subsequently etching. A frequency shift of $-34\,\mathrm{cm}^{-1}$ was observed for each total film thickness.

constants, m is the mass of the oxygen atom, and θ is the bridging bond angle of Si–O–Si. If m is in kg, a is in $\mathrm{N\,m}^{-1}$, and the multiplying constant $a = 5.305 \times 10^{-12}$, then the expression yields ω_4 in cm^{-1}. A compilation of data[16] on materials, where θ has been measured directly by methods such as electron or X-ray diffraction, shows that in a very good approximation, for $\theta \leq 150°$, $\alpha = 582\,\mathrm{N\,m}^{-1}$ and $\beta = 264\,\mathrm{N\,m}^{-1}$. Equation (1) then enables us, with some confidence, to estimate Si–O–Si bond angles based on measured IR absorption frequencies. A shift in ω_4 from $1078\,\mathrm{cm}^{-1}$ to $1044\,\mathrm{cm}^{-1}$ would imply a decrease in Si–O–Si bond angle from 144° to 129°. The Si–O–Si bond angle in planar three-member rings has been estimated to be 130.5°.[16] Therefore, one likely explanation of such a strong reduction of the shift of ω_4 would be the reduction of ring size from six-membered rings to planar three-member rings. The present model is consistent with the fact that θ_3 is calculated at 130.5° in Fig. 9.

The frequency ω_4 of wet-SiO_2 is different from that of dry-SiO_2, and it decreases with increasing thickness of a-SiO_2 on silicon.[17–19] Therefore, it would be incorrect to compare frequency between dry-SiO_2 and wet-SiO_2 without considering film thickness. Figure 10 presents the frequency variation of the ω_4 peak as a function of SiO_2 thickness. The measurements started with a complete as-deposited film and the thickness was reduced by chemical etching performed in a series of steps. After each step, both the thickness and the IR absorption were measured. A thickness of 0 nm corresponds to the interface between a-SiO_2 and the silicon substrate. Open and closed circles denote the ω_4 values of dry-SiO_2 and wet-SiO_2 versus thickness after etching, respectively. Both plots are almost on the same curve except in the region near the interface with the silicon substrate, where the frequency decreased steeply for dry-SiO_2, but gradually for wet-SiO_2. Open and closed squares present the ω_4 values of dry-SiO_2 and wet-SiO_2 subjected to 67 MeV Br irradiation at an accumulated dose of $3 \times 10^{14}\,\mathrm{cm}^{-2}$, respectively, again versus thickness after etching. Note that the frequency shift from pristine to irradiated sample is in the vicinity of $-34\,\mathrm{cm}^{-1}$ regardless of the thickness and type of a-SiO_2. It is concluded that the average bond angle of Si–O–Si and the ratio of planar three-membered rings in dry-SiO_2 is almost the same as those in wet-SiO_2, except within a few tens of nm of the interface between silicon and a-SiO_2. These data also show that, except for a few nm close to the interface, both the films and the irradiation effects are the same throughout the entire thickness investigated.

The data shown in this article covers the effects of a wide range of ion species, energies, and fluences of the structure of a-SiO_2. In order to compare one ion mass with another, some scaling of the ion dose is required. In particular, we would like to compare measurements at an accumulated fluence where individual cylinders are just beginning to overlap. This fluence can be estimated using an analytical formula[20] for the radial profile of the spatial energy deposition. Figure 11 shows a plot of some experimental data in the high-velocity-ion regime.[21,22] The radius R_d of the damaged cylinder is estimated at 65% of the incident energy. Here we define the minimum dose as the dose required to cover the surface with damaged zones (MDDZ), estimated with using the formula,

$$\mathrm{MDDZ}\ (\mathrm{cm}^{-2}) = 0.65/\{(10^{-7}R_\mathrm{d})^2\pi\}. \qquad (2)$$

By using R_d values of 1.5, 1.9, 2.8, 2.5, 3.4, and 2.7 nm for 2 MeV Li, 4 MeV C, 30 MeV Si, 35 MeV Se, 67 MeV Br and 78 MeV I, the MDDZ values were estimated to be

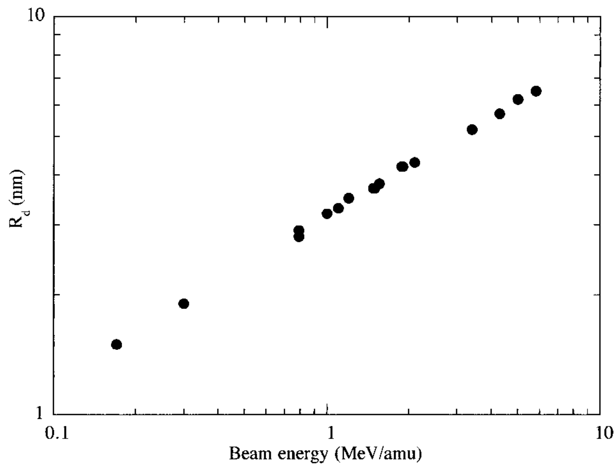

Fig. 11. Plot of cylinder radius, R_d, in which 65% of dE/dx is deposited against beam energy. The data were cited from a ref. 6.

9.8×10^{12}, 8.0×10^{12}, 6×10^{12}, 5.5×10^{12}, 2.7×10^{12}, and $5.1 \times 10^{12}\,\text{cm}^{-2}$, respectively. These values are plotted in Fig. 5 using open triangles, squares, circles, diamonds and reversed triangles, respectively. The estimated values of etching rate at MDDZ from Fig. 5 were re-plotted in the ordinate on the left-hand side using closed circles against the peak shift in ω_4 depicted in Fig. 12. We also plotted the hole diameters of the tracks etched with 48% hydrofluoric acid for 45 s. against the peak shift in ω_4 (open circles) in the ordinate on the right-hand side. Details on the ion species and their energy values are given in Fig. 12 and denoted by arrows.

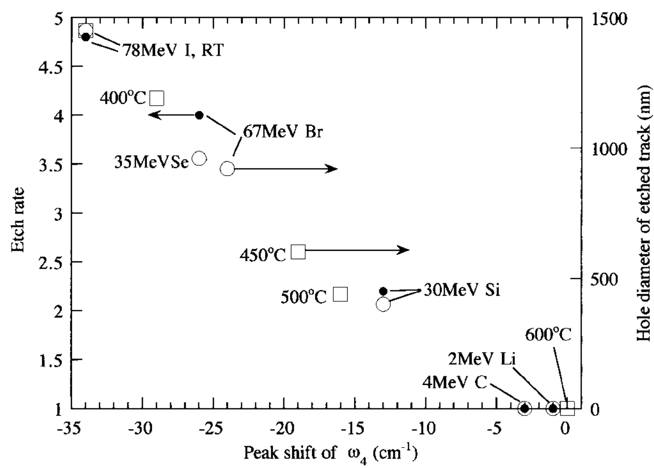

Fig. 12. Plot of etching rate (right-hand side) and diameter of the etched tracks (left-hand side) against peak shift in ω_4. Relative etching rate was determined from the step height between the irradiated and masked parts of wet-SiO_2 after etching. Closed circles denote the estimated relative etch rate of wet-SiO_2 subjected to irradiation. Ion species and their energy are shown. The diameter of the etched track represented by open circles was determined with SEM observation of a-SiO_2 plates subjected to irradiation, then etched with 48% hydrofluoric acid. Wet-SiO_2 films were also subjected to the same treatment to determine ω_4. The ion species and their energy are also shown. The annealing behavior of the latent track was examined and denoted by open squares. Both a-SiO_2 plates and wet-SiO_2 films subjected to 78 MeV I irradiation were annealed at 400°C, 450°C, 500°C and 600°C, subsequently etched with 48% hydrofluoric acid, and subjected to SEM of the etched tracks and IR measurement to determine ω_4.

Figure 12 shows the plots of both etching rates and hole diameter versus IR peak shift, as evaluated at MDDZ. The etch rate at MDDZ was estimated from Fig. 5, and is shown as solid symbols plotted on the left axis. The hole diameters are plotted as open symbols on the right axis. Heavy ions such as Se, Br and I, which upon etching introduce clear individual holes on a-SiO_2, are observed to introduce a large shift in ω_4 at MDDZ. It is concluded from the results that even the passage of a single Se, Br or I ion creates a latent track where the shift in ω_4 is at least $-20\,\text{cm}^{-1}$.

These data are compared directly with the annealing results of 78 MeV I-irradiated samples: the open circles denote the diameter of holes irradiated with 78 MeV I, and then annealed and etched versus the shift in ω_4. The annealing was performed prior to etching and IR absorption measurement. The maximum shift in ω_4 of the wet-SiO_2 subjected to 78 MeV I irradiation at an accumulated dose of $5.1 \times 10^{12}\,\text{cm}^{-2}$ (MMDZ) reached $-34\,\text{cm}^{-1}$. An increase in ω_4 and a decrease in the hole diameter of the etched tracks are simultaneously observed with increasing annealing temperature. The open squares (annealing) fall on the same line as the open circles (different ion masses) which strongly implies that the shift in ω_4 in the latent tracks correlates with the etching efficiency of those tracks. Moreover, the etching rate (closed circles in Fig. 12) complements determine the data on the etched tracks shown in Fig. 9. In our previous study, we could not determine the relationship between the concentration of E$'$ center as the paramagnetic center and etching rate. Also there was no relationship between oxygen loss induced by ion irradiation and etching rate for a-SiO_2. Thus, it is concluded that etching efficiency strongly correlates to the shift in the frequency ω_4.

We discuss why three-membered rings is introduced by irradiation. Formally, Galeener reported that concentration of the three-membered rings increases with increasing fictive temperature which implies a higher temperature at which a-SiO_2 is allowed to reach an equilibrium state before a rapid quench to room temperature. Vollmayr *et al.*[23] investigated by molecular-dynamic computer simulations how in silica the properties of the resulting glass depend on fictive temperature. They found that the distribution of the angle Si–O–Si changes significantly with fictive temperature. The position of the peak for the Si–O–Si angle moves to smaller angles and becomes much broader when the fictive temperature increases. Since this angle provides the relative orientation between two neighboring tetrahedra, this observation is in accordance with the picture of the densifying network, when the temperature increases. They also calculated the distribution of the size of the rings and found that in this case the distribution of the intrinsic size of the rings depends significantly on the temperature. Moreover, this distribution becomes significantly broader when the temperature is increased and that the main change is the increase in the number of short rings. They investigated the temperature dependence of the vibration spectrum. The peak position of ω_4 in the vicinity of $1100\,\text{cm}^{-1}$ was shifted toward the lower frequency side with increasing fictive temperature. Toulemonde *et al.*[6] mathematically estimated lattice temperature plotted against time at a distance of 1 nm to 8 nm from the ion path in SiO_2. In the calculation, a krypton beam energy of 3.4 MeV/amu corresponding to an

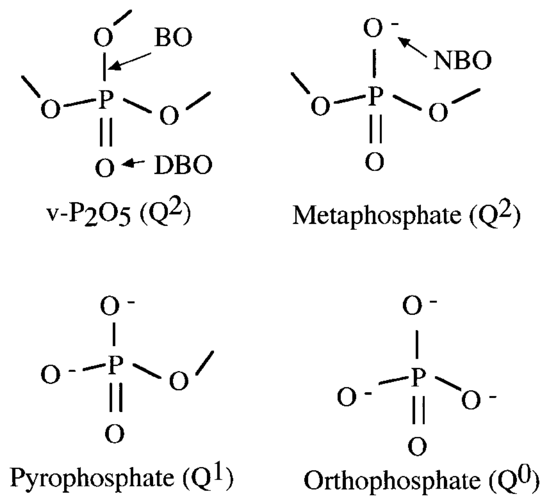

Fig. 13. Four kinds of phosphate glass. Double bonding oxygen, bonding oxygen and non bridging oxygen are denoted by DBO, BO and NBO, respectively.

electronic stopping power of 12 keV/nm was used. The temperature increased up to 3223 K within 10^{-14} s and decreased within 10^{-10} s at a distance of 1 nm. The calculation also indicated that flash heating and quenching were induced by ion irradiation.

4.2 ZnP glass

The Q^n notation for phosphate groups in XPS is widely adopted,[24] where n is the number of bridging oxygen atom per PO_4 tetrahedron, as shown schematically in Fig. 13. The binding energies of Q^0, Q^1, Q^2 and Q^3 in the P_{2p} spectra have been reported to be 132.5, 133.5, 134.5 and 135.5 eV, respectively.[25] In the O_{1s} spectra, the binding energy of the non-bridging oxygen (NBO) is very close to the binding energy of oxygen with double bonds (DBO) but the width of the NBO signal was narrower than that of the bridging oxygen (BO) signal. The binding energy of the BO is 2 eV higher than the binding energies of NBO and DBO.[26]

Using the above assignments, we now discuss the XPS information. The shape of the P_{2p} spectra shown in Fig. 7 is attributed to mainly Q^1 and Q^2. We notice that Q^2 transformed to Q^1 with ion irradiation. This finding implies that scission of P–O bonds occurs upon ion irradiation. In the O_{1s} spectra, a shoulder attributed to BO and observed at about 534 eV disappeared with ion bombardment. We assume that the bridging oxygen transformed to the non-bridging oxygen with ion bombardment, as suggested by the O_{1s} spectra.

Results of Raman spectroscopy also give some evidence of the scission of P–O bonds. Raman bands at 697 cm^{-1}, 1206 cm^{-1} and 1270 cm^{-1} have been well examined and assigned to P–O–P stretching modes in Q^2 species, and to the symmetric and asymmetric stretching motions of the two non-bridging oxygen atoms bound to phosphorus atoms in the Q^2 phosphate tetrahedra, respectively.[24] The 970 cm^{-1} and 1048 cm^{-1} bands have been assigned to the symmetric stretching mode of the non-bridging oxygen atoms in the Q^0 tetrahedra and the motion of the non-bridging oxygen atoms in the Q^1 tetrahedra, respectively.[24] New bands observed for the irradiated sample in the region of 1000 cm^{-1} are assigned to Q^0 and Q^1. XPS and Raman data thus imply that fast ions induce linear trails of P–O bond scission. In contrast, no change was induced in the environment of zinc atoms. Recently, the structure of BP-1 glass ($26BaO:65P_2O_5:4.3Na_2O:4.6SiO_2$) has been investigated by Raman spectroscopy and it was confirmed that Q^2 signals are transferred to Q^1 and Q^0 signals with ion irradiation, a finding that provides additional support to the present conclusion on ZnP glass.

5. Conclusions

We were able to create individual cones in a-SiO_2 and zinc phosphate glass by ion irradiation followed by chemical etching. We examined the mechanism underlying the increase in the etch rate in the latent track. It was found that a decrease in the average bond angle of Si–O–Si, deduced from the evolution of ω_4, is responsible for the high etching rate. The average bond angle of Si–O–Si was reduced to 129° corresponding to the bond angle of planar three-membered rings. These three-membered rings are likely introduced by flash heating and quenching following the passage of swift heavy ions. In ZnP glass, a decrease in the number of bridging oxygen atoms and a transformation of Q^2 species to Q^1 and Q^0 species imply the scission of P–O bonds. By comparison, no change was observed by XPS around Zn atoms. It is concluded that the increase in the etching rate of latent tracks is related to scission of P–O bonds and not to the structural change of the surroundings of zinc atoms.

Acknowledgements

We thank S. Ito and N. Sugimoto for the preparation of ZnP glass, P. Bérichon and R. Gosselin for expert assistance in the operation of the tandem accelerator and S. Poulin for XPS measurement. This work was supported by the Budget for Nuclear Research approved by the Atomic Energy Commission from the Ministry of Education, Culture, Sports, Science, and Technology of Japan.

1) R. L. Fleischer: Mater. Res. Soc. Bull. **20** (1995) 17.
2) G. Fiedler, J. Aschenbach, W. Otto, T. Rautenberg, U. Steinhauser and G. Siegert: Nucl. Instrum. & Methods **147** (1977) 35.
3) V. E. Kopchenov and V. A. Nikolaev: Nucl. Tracks Radiat. Meas. **11** (1986) 221.
4) R. L. Fleischer, P. B. Price and R. M. Walker: *Nucl. Tracks in Solids-Principles and Applications* (University of California Press, Berkley, 1975).
5) G. Bonfiglioli, A. Ferro and A. Monjoni: J. Appl. Phys. **32** (1961) 2499.
6) M. Toulemonde, J. M. Costantini, Ch. Dufour, A. Meftah, E. Paumier and F. Studer: Nucl. Instrum. & Methods Phys. Res. **B 116** (1996) 37.
7) R. L. Fleischer: Mater. Res. Soc. Bull. **20** (1995) 17.
8) R. Brückner: J. Non-Cryst. Solids **5** (1970) 123.
9) K. Awazu, S. Ishii, K. Shima, S. Roorda and J. L. Brebner: Phys. Rev. **B 62** (2000) 3689.
10) K. Awazu, S. Ishii and K. Shima: Jpn. J. Appl. Phys. **39** (2000) 7058.
11) A. Pasquarello and R. Car: Phys. Rev. Lett. **80** (1998) 5145.
12) F. L. Galeener: Solid State Commun. **44** (1982) 1037.
13) M. D. Newton and G. V. Gibbs: Phys. Chem. Minerals **6** (1980) 221.
14) P. N. Sen and M. F. Thorpe: Phys. Rev. **B 15** (1977) 4030.
15) A. Lehmann, L. Schumann and K. Hübner: Phys. Status. Solidi **B 117** (1983) 689.
16) R. A. B. Devine: J. Non-Cryst. Solids **152** (1993) 50.
17) H. R. Philipp: J. Appl. Phys. **50** (1979) 1053.

18) M. K. Gunde and B. Aleksandrov: Appl. Spectrosc. **44** (1990) 970.
19) I. W. Boyd and J. I. B. Wilson: Appl. Phys. Lett. **50** (1987) 320.
20) A. E. Geissberger and F. L. Galeener: Phys. Rev. **B 28** (1983) 3266.
21) M. P. R. Waligorski, R. N. Hamm and R. Katz: Nucl. Tracks Radiat. Meas. **11** (1986) 309.
22) A. Meftah, F. Brisard, J. M. Costantini, E. Dooryhee, M. Hage-Ali, M. Hervieu, J. P. Stoquert, F. Studer and M. Toulemonde: Phys. Rev. **B 49** (1994) 12457.
23) K. Vollmayr, W. Kob and K. Binder: Phys. Rev. **B 54** (1996) 15808.
24) R. K. Brow, D. R. Tallant, S. T. Myers and C. C. Phifer: J. Non-Cryst. Solids **45** (1995) 191.
25) R. Gresch, W. Müller-Warmuth and H. Dutz: J. Non-Cryst. Solids **34** (1979) 127.
26) R. Brückner, H. U. Chun, H. Goretzki and M. Sammet: J. Non-Cryst. Solids **42** (1980) 49.
27) T. Yamauchi: private communication.